

Multiparameter Synchronous Measurement With IVUS Images for Intelligently Diagnosing Coronary Cardiac Disease

Yankun Cao^{ID}, Ziqiao Wang^{ID}, Zhi Liu^{ID}, *Member, IEEE*, Yujun Li^{ID}, *Member, IEEE*, Xiaoyan Xiao^{ID}, Longkun Sun^{ID}, Yang Zhang^{ID}, Haixia Hou^{ID}, Pengfei Zhang^{ID}, and Guang Yang^{ID}, *Member, IEEE*

Abstract—Intravascular ultrasound (IVUS) can provide high-resolution cross-sectional images of coronary arteries, showing detailed information of the vascular lumen, tube wall, and athermanous plaques, which is helpful for the discovery or identification of early coronary atherosclerotic plaques. Multiple parameters extractable from the IVUS image can help the cardiologist analyze the pathology and assist in disease diagnosis and postoperative treatment. Typically, cardiologists manually label the intima and adventitia in the IVUS image, and obtain a limited number of parameters through the IVUS instrument, which is time consuming and labor-intensive. To assist the cardiologist in automatically obtaining more clinically relevant value parameters, a fully automatic IVUS multiparameter extraction framework is proposed. Based on the intima and adventitia obtained by DeepLab V3+, we propose a targeted noise reduction preprocessing framework adapted to IVUS. The framework implements the basic parameter extraction of IVUS through two newly proposed algorithms. And through the standard medical formula, the basic parameters are converted into 10 standard medical indicators. Standardized medical indicators are obtained by clinically relevant basic parameters. In terms of accuracy, this article used a clinical database obtained from Qilu Hospital of Shandong University and compared the results of the framework with the gold standard of cardiologists. The relative error of continuous IVUS main parameters between frames did not exceed 10.10%. The relative error of independent IVUS did not exceed 10.03%. Based on the distribution consistency of the

parameters and the gold standard, a Bland-Altman plot of the parameters is proposed. It was verified that this distribution is basically in line with the gold standard of cardiologists. The algorithm in this article obtained a total of 10 parameters, far exceeding the parameters obtained by cardiologists and traditional IVUS machines. Its accuracy and speed can also meet the requirements of cardiologists for clinical diagnosis.

Index Terms—Bland-Altman plot, Deeplab v3+, intravenous ultrasound, multiparameter measurement, vascular wall segmentation.

I. INTRODUCTION

IN RECENT years, the incidence of cardiovascular diseases has increased, and it has become a significant disease that endangers human health. How to diagnose and treat cardiovascular disease is particularly important. In cardiovascular imaging, intravascular ultrasound (IVUS) has been widely accepted as the gold standard for coronary atherosclerotic disease as well as vessel lesions. This imaging technique is broadening its application in interventional therapy since IVUS can provide cross-sectional information of the vessel with high spatial and temporal resolution. The cross-sectional information contains not only the lumen, which is the main provision from angiography but also information on the intima, vessel wall, and adventitia. An IVUS image is shown in Fig. 1.

In addition, IVUS is capable of evaluating the severity and vulnerability of atherosclerotic plaques through derived parameters, including plaque burden (PB), eccentric index (EI), remodeling index (RI), and others. However, to calculate these parameters, the IVUS catheter needs to be pulled back along the vessel by the IVUS equipment at a constant speed to acquire the scenario of pan vessel lesions. Take the typical settings of this scanning procedure where the pullback speed is 0.5 mm/s, and the frame rate is 30 frames/s. That will be 6000 frames for a 10 mm-long lesion, and it would be laborious to manually delineate the intima and adventitia on each frame as the basic input for the parameters as mentioned earlier.

Currently, the analysis and identification of intravascular plaques with IVUS are necessary for the diagnosis of cardiovascular disease. Through IVUS observation, calcified plaques, fibrous plaques, and different levels of vulnerable plaque can be treated accordingly. Various IVUS parameters have significant reference value for predicting the form of plaque and

Manuscript received July 9, 2020; revised September 12, 2020; accepted October 16, 2020. Date of publication November 24, 2020; date of current version September 9, 2021. This work was supported in part by the Major Fundamental Research of Natural Science Foundation of Shandong Province under Grant ZR2019ZD05, and in part by the Joint Fund for Smart Computing of Shandong Natural Science Foundation under Grant ZR2020LZH013. The Associate Editor coordinating the review process was Dr. Amitava Chatterjee. (Yankun Cao and Ziqiao Wang are co-first authors.) (Corresponding authors: Yujun Li and Pengfei Zhang.)

Yankun Cao is with the School of Software, Shandong University, Jinan 250101, China.

Ziqiao Wang, Zhi Liu, and Yujun Li are with the School of Information Science and Engineering, Shandong University, Qingdao 266237, China (e-mail: liyujun@sdu.edu.cn).

Xiaoyan Xiao is with the Department of Nephrology, Qilu Hospital of Shandong University, Jinan 250012, China.

Longkun Sun and Pengfei Zhang are with the Department of Cardiology, Qilu Hospital, Cheeloo College of Medicine, Shandong University, Jinan 250012, China (e-mail: pengf-zhang@163.com).

Yang Zhang is with the Department of Radiology, Qilu Hospital of Shandong University, Jinan 250012, China.

Haixia Hou is with the Centre of Information Security, Beijing University of Posts and Telecommunications, Beijing 100876, China.

Guang Yang is with the National Heart and Lung Institute, Imperial College London, London SW7 2AZ, U.K.

Digital Object Identifier 10.1109/TIM.2020.3036067

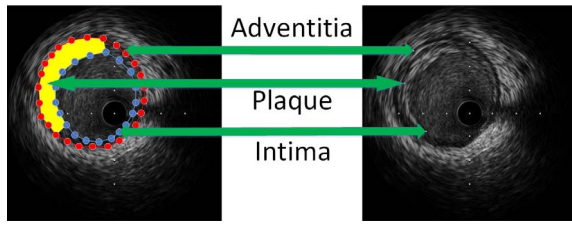


Fig. 1. IVUS original image.

observing intravascular lesions. To help cardiologists diagnose and save cardiologists' time, a fully automatic IVUS multiparameter extraction framework is needed. At present, most of the relevant papers on IVUS stop at intima and adventitia segmentation or numerical analysis of IVUS parameters that have been manually extracted by cardiologists. IVUS medical instruments can only extract a small number of parameters, which is not conducive to cardiologists conducting a variety of studies on lesions. For this reason, a framework that includes a presegmentation algorithm and automated extraction of parameters is built. In this framework, we first need to outline the intima and adventitia according to DeepLab v3+ [1], and then innovatively design and extract multiple parameter algorithms, which can quickly calculate multiple medical parameters in batches.

The remainder of this article is organized as follows. In Section II, related works are presented. The methods of the fully automatic IVUS multiparameter extraction framework are detailed in Section III. The IVUS database and the experimental setup are shown in Section IV. The results and discussion are presented in Section V. Finally, the conclusion is presented in Section VI.

II. RELATED WORKS

Currently, ultrasound images have shown a notable role in the analysis of vascular plaque and assisted diagnosis [2]–[4]. In the IVUS fully automatic multiparameter extraction framework, the first step is image segmentation. The typical convolutional neural network shows great results in IVUS segmentation. IVUS-Net [5] is based on the traditional FCN to segment the IVUS images. The final experimental results reached 0.90 and 0.26 on the Jaccard Measure and Hausdorff Distance indicators. However, IVUS-Net still does not further extract the subsequent parameter details but stops at segmentation. At the same time, the data set used by IVUS-Net is 20 MHz, and today's medical general-purpose instruments are 40 MHz, and the image quality is more detailed and richer.

Many papers have presented practical methods in image segmentation. A basing sparse representation framework and dynamic directional active contour model obtain a 2.407% area difference [6]. Additionally, using a deep convolutional neural network obtains a concordance correlation coefficient of approximately 0.97 in lumen area evaluation and 0.93 in PB evaluation [7]. A new graph-based approach for the segmentation of luminal and external elastic lamina (EEL) surface of coronary vessels is presented [8]. In [8], the mean and standard deviation of the root mean square area errors

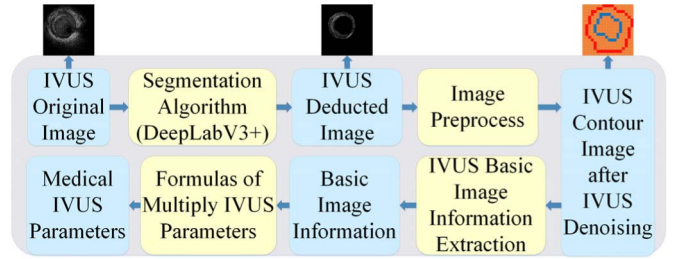


Fig. 2. Fully automatic IVUS multiparameter extraction framework.

for the luminal and EEL surfaces were $1.12 \pm 0.67 \text{ mm}^2$ and $2.35 \pm 1.61 \text{ mm}^2$, respectively. And a novel multiagent image interpretation system has been developed [9], which also obtains satisfactory effects. In addition, Vercio *et al.* [10] use random forests to segment the vessel wall and Rezaei *et al.* [11] use the k nearest neighborhood to segment plaque automatically, and the result also demonstrates the advantages. Taki *et al.* [12] show that the geometric deformable model outperforms the parametric deformable model for automated the segmentation of IVUS coronary artery images.

Many published results show that IVUS automatic segmentation technology reaches a reliable level. However, most of the article's evaluation indices do not list the areas between the intima and the adventitia. Due to the significant difference in image segmentation between the intima and the adventitia, it may be challenging to obtain a good segmentation result, and it is necessary to address this problem squarely. Therefore, after the segmentation algorithm, it is imperative to perform secondary processing on the image. Another important reason is that the data sets used in other articles include a small number of images. Manual marking, especially in the area between the intima and the adventitia, may have errors, which will result in a low level of mean intersection over union (mIoU). Using fewer validation sets may result in an insufficient generalization of the results. Therefore, the framework experiment uses a large number of IVUS images for validation. Using a larger quantity of data, its authenticity is closer to the real clinical environment. There are no related papers or algorithms to study parameter extraction.

III. METHODS

The standardized medical indicators of the IVUS consist of basic IVUS digital image information. To obtain deep IVUS parameters, the basic IVUS parameters extractable from in IVUS images are needed. However, the existing parameter calculation tools are strictly dependent on the doctor's manual labeling of the intima and adventitia, which are time consuming and can only be labeled in a single frame. In this article, an algorithm framework for fully automatic extraction of IVUS parameters is proposed. As shown in Fig. 2, first, the framework divides the intima and adventitia of the original IVUS image. The original image is then subtracted from the label image to obtain an image having only the region of interest (ROI). For image denoising, framework preprocessed the deduced image. Due to the particularity of the data noise,

this article adopts a method different from other medical image denoising methods [13]–[15]. Subsequently, a new parameter calculation algorithm is proposed to obtain the basic IVUS parameters, and the deep parameters are obtained subsequently.

A. Segmentation

In recent years, machine learning algorithms and neural networks have demonstrated outstanding potential and influence in various fields. Due to the emergence of FCN [16], the field of neural networks has shifted from traditional image segmentation to semantic segmentation. PSPNet [17] may be more suitable because of its feature map processing of images from rough global detail features to local detail features. Similar to FCN, SegNet [18] also performs upsampling and downsampling on images, but it uses pooling indices to maintain the integrity of high-frequency details. As a classic medical segmentation network, U-Net [19] is suitable for most biomedical segmentation fields, but since it is not trained in the data sets mentioned above, U-Net is not included in the network comparison. CRF-RNN [20] has been improved based on FCN. The conditional random field has been added to the FCN to improve image refinement. At the same time, the learning process is regarded as an RNN [21] for training. HR-Net has attracted everyone's attention in the superior performance of Cityscape and the performance in various data sets, but it has not been applied by the public. DeepLabV3+ is a state-of-the-art semantic segmentation neural network. It combines the advantage of spatial pyramid pooling and the encoder–decoder framework. DeeplabV3+ [1], based on DeepLabV3 and inspired by Xception, created a new encoder–decoder module. DeepLabV3+ fusion multiscale information optimized the network structure of the encoder–decoder. Finally, DeepLab V3+ improved the speed and robustness of the encoder–decoder; thus, DeepLabV3+ obtained the state-of-the-art in PASCAL VOC 2012. Therefore, deeplab V3+ is selected as our segmentation network in this article.

B. Image Preprocessing

Digital images consist of discrete pixels that are susceptible to noise and cause discontinuities, overlap in the area. The framework performs noise reduction and gradient processing on the segmented image to reduce noise interference and prepare for subsequent parameter acquisition. The label image is obtained by DeepLabV3 + neural network segmentation or manual segmentation, as shown in Fig. 3(a).

The unmarked area is subtracted from the original image to obtain a ROI. Due to poor segmentation, some IVUS-tagged images do not perfectly separate the intima and adventitia, as shown in Fig. 3(b). Therefore, the image needs to be preprocessed to solve the image noise problem and the overlap of the intima and adventitia.

In Fig. 3(b), the blue square represents the intima, the red square represents the adventitia, and the green square represents an indistinguishable area composed of intima and adventitia overlap. Based on this, an expansion algorithm is proposed in this article to extend the overlap area with width

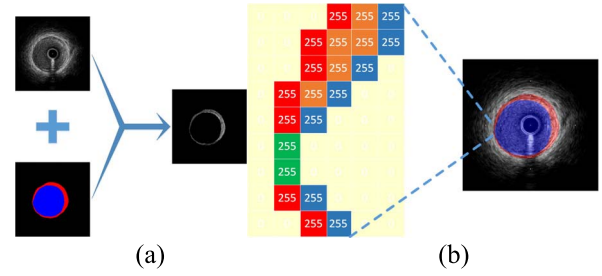


Fig. 3. (a) IVUS deduced image. (b) IVUS inseparable image.

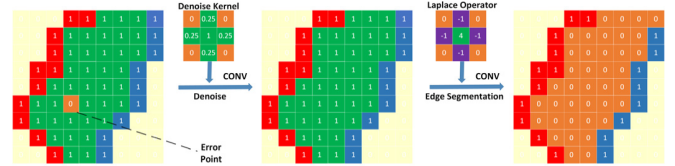


Fig. 4. IVUS discrete point noise.

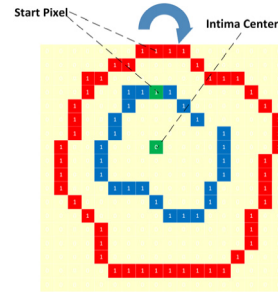


Fig. 5. Initial point of matrices' aligns.

one and binarize the original image to extract the basic IVUS parameters. After the expansion algorithm, we obtained the IVUS image with no obvious areas. However, the IVUS image still had some noise caused by pixels with a gray value of zero. To eliminate noise between the intima and the adventitia, a filter to denoise the edge image was designed in this article. The denoised image was then convolved with the Laplacian. The Laplace operator is shown in Fig. 4.

C. Multiparameter Measurement of IVUS

1) Basic Image Information Extraction:

a) *Save the intima and adventitia matrices:* After image preprocessing, the segmented adventitia and intima matrices are stored in corresponding matrices for basic parameter extraction. The connection of two matrices' first point can be made perpendicular and through the center of the intima. Intima matrix and adventitia matrix are in a clockwise. As shown in Fig. 5.

The storage algorithm is described in detail below. First, starting from the first line, the row-by-row query selects the first pixel in which the pixel gray value is not 0 in the edge image, and the selected pixel is located in the adventitia matrix. Use this pixel as the first point to be saved in the adventitia matrix. Then, the adjacent pixel of the first pixel is also stored as the second pixel in the adventitia matrix.

The neighboring pixel is on the right side of the first pixel, and the new neighboring pixel does not appear in the adventitia matrix. The adjacent pixels of the second pixel are then found until the entire adventitia matrix is held in the adventitia matrix. The adventitia matrix pixel preservation rule is as shown in the following equation:

$$\begin{aligned} \text{Dist}(P_{\text{adv}}(i), P_{\text{adv}}(i-1)) &\leq \sqrt{2} \\ \text{GrayValue}_{\text{adv}}(i) &= 1 \\ P_{\text{adv}}(i) &\neq P_{\text{adv}}(i-2). \end{aligned} \quad (1)$$

In (1), adv is the adventitia, Dist is the distance, and P is the matrix point.

After the adventitia pixels are stored in the adventitia matrix, the next step is to store the intima pixels in the intima matrix. The algorithm also preserves the intima pixels in a clockwise direction, which is stored in the same way as the adventitia matrix. For the first pixel of the intimal matrix and the adventitia matrix to be in the same column of the image, adjustments are needed. First, the center point of the intima must be calculated. The calculation formula is defined as

$$(\text{IC}_x, \text{IC}_y) = \frac{1}{n} \sum_{i=1}^n (\text{IM}_x(i), \text{IM}_y(i)). \quad (2)$$

In (2), n is the length of the intima matrix. IM_x is the row index of the intima matrix and IM_y is the column index of the intima matrix. IC_x is the row index of the intima center; IC_y is the column index of the intima center. After obtaining the intima center, the final step is to adjust the intima matrices' first element, adventitia matrices' first element, intima center in a line, and ensure that the elements are clockwise.

b) *Minimum distance rotating segment algorithm*: The above algorithm yields the intima matrix, the adventitia matrix, and the intima center. This article next proposes an algorithm that can obtain the plaque thickness between the intima and the adventitia. The method for obtaining plaque thickness is to establish a ray from the center of the intima to the point of the intima element. The intersection of the ray and the adventitia matrix is the point at which the intimal point is paired. The distance between the two is the wall thickness. The linear equation of the ray is shown in the following equation:

$$\frac{y - \text{IM}_y}{\text{IM}_y - \text{IC}_y} = \frac{x - \text{IM}_x}{\text{IM}_x - \text{IC}_x}. \quad (3)$$

The starting point of the ray is the center of the intima. The outer extends outward then passes through the intimal matrix and the adventitia matrix. However, due to the discreteness of the digital image, it is difficult to find a point in the adventitia matrix that can perfectly intersect the ray. So algorithm chooses the point closest to the ray in the adventitia matrix (Fig. 6).

The distance from the point to the ray is shown in the following equation:

$$\begin{aligned} A &= \text{IC}_y - \text{IM}_y \\ B &= \text{IM}_x - \text{IC}_x \\ C &= \text{IC}_x \times \text{IM}_y - \text{IC}_y \times \text{IM}_x \\ d &= \left| \frac{Ax + By + C}{\sqrt{A^2 + B^2}} \right| \end{aligned} \quad (4)$$

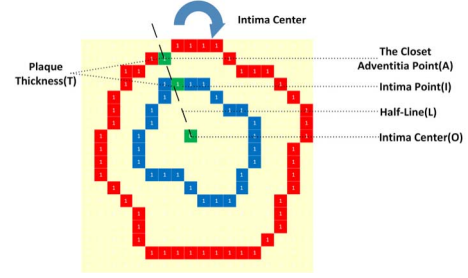


Fig. 6. Select the minimum distance point.

where d represents the distance from the ray to the adventitia matrix point, and x and y represent the iterative adventitia matrix coordinates. $A-C$ are linear general formula coefficients. The goal is to obtain the plaque thickness at each point of the intima matrix. Then, iterate through all the adventitia matrix points of each intimal matrix point and obtain the shortest distance. As shown in the following equation:

$$\begin{aligned} (\text{PTAM}_x, \text{PTAM}_y) &= \arg \min d \\ (\text{PTAM}_x, \text{PTAM}_y) &= \arg \min \left| \frac{Ax + By + C}{\sqrt{A^2 + B^2}} \right| \\ \text{PT} &= \frac{\sqrt{(\text{PTAM}_x - \text{IC}_x)^2 + (\text{PTAM}_y - \text{IC}_y)^2}}{\text{ratio}} \end{aligned} \quad (5)$$

where PTAM_x and PTAM_y represent the adventitia point. PT represents the plaque thickness and ratio represents the unit conversion from pixel numbers to mm. Through manual measurement, in 256×256 images, the ratio was 28.

Based on (5), a new iterative algorithm is designed to calculate plaque thickness. First, select an adventitia point connecting line through the adventitia pixel at the center of the intima. Then, when the intima pixel moves one unit clockwise, the adventitia pixel points also move in time. The distance between the adventitia pixel point and the ray at this time will gradually decrease and then increase. When the distance suddenly increases, it means that the distance from the previous point is the smallest. The distance of the ray is chosen to be the plaque thickness of the intima pixel point. In addition, moving the intimal unit clockwise in turn will result in a corresponding series of adventitia pixels and plaque thickness. Compared with the traditional iteration algorithm $O(n^2)$, the complexity of the algorithm is reduced to $O(n)$, which reduces the running time. The structure of the algorithm is shown in Fig. 7.

c) *Double line segment coverage algorithm—plaque area*: In clinical diagnosis, cardiologists are interested in areas where the plaque thickness is greater than 1.2 mm. To calculate the plaque area with plaque thickness greater than 1.2 mm, a new double line segment coverage algorithm is proposed in this article. It is known that in a 256×256 pixels are equal in length to 1 mm. First, the initial segment and the ending segment are determined. When the plaque thickness is greater than or equal to 1.2 mm, the algorithm sets the plaque segment as the starting segment and then searches for

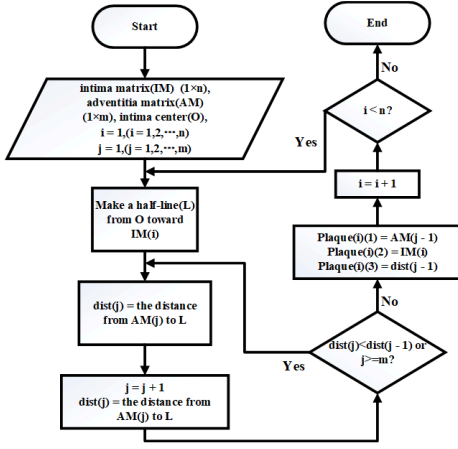


Fig. 7. Minimum distance rotating segment algorithm.

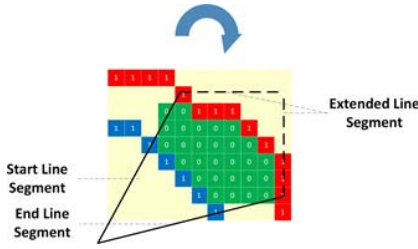


Fig. 8. Double line segment coverage algorithm.

the segment in turn. If the thickness of the segment is less than 1.2 mm, the plaque fragment is set as the end segment. Thereafter, the algorithm intersects the triangular region with the rectangular region. The triangle area consists of a start point and an endpoint. The triangular area is composed of the start segment and an end segment. The algorithm used the start segment's adventitia point and end segment's adventitia point to make a rectangle's diagonal. Therefore, the rectangular area is also obtained. Finally, we use the overlap region and the deducted image to obtain all of the plaque matrices, as shown in Fig. 8. It should be noted that the angle between the starting line segment and the ending line segment should be less than or equal to 90° through the algorithm. When the angle is less than or equal to 90° , the coverage area does not lose plaque points. After that, the algorithm stores all of the pixels in the image into a new plaque matrix. The algorithm then looks again at the start and endpoints until it traverses all plaque regions. With this algorithm, the plaque area can be obtained.

2) *Calculation of Multiparameters*: In clinical diagnosis, there are many parameters that doctors are interested in. The following briefly introduces the following parameters.

a) *EI*: The EI shows the relative error level from the center to the lumen. The EI can reflect the effects of different metal supports [22]

$$EI = \frac{\max LD - \min LD}{\max LD}. \quad (6)$$

In (6), maxLD and minLD represent the maximum lumen diameter and the minimum lumen diameter, respectively. The lumen diameter is calculated similar to the rotation segment

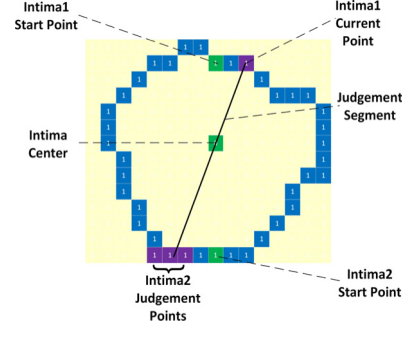


Fig. 9. Diameter extraction.

minimum distance algorithm. First, the intima matrix named intima 2 and the original intima matrix named intima 1 were copied. The initial points of the two intimal matrices were in the same column, and the initial points' column index was the same as the intima center column index. However, intima 1 was above the intima center, and intima 2 was below the intima center. We made a ray from intima 1 to the intima center and calculated the distance from the intima 2 current judgment point to judgment. Then, we selected the judgment point to the next point in intima 2 and calculated the distance as well. When the current judgment point's distance was smaller than the last judgment point's distance, the last judgment point was selected as the nearest point. The diameter was the distance from the nearest point to the intima 1 point. Finally, the intima's entire diameter can be obtained, and we can calculate the EI parameter. The circle diameter and the method of diameter extraction are shown in Fig. 9.

b) *PB*: The PB parameter can provide considerable information regarding atherosclerosis. Many cardiovascular risk factors and carotid plaque components are associated with carotid PB [23]. The PB can predict possible heart disease [24]. The PB calculation equation is shown in the following equation:

$$PB = \frac{EEMCSA - \text{Lumen CSA}}{EEMCSA} \quad (7)$$

where PB represents the PB. Lumen CSA is the area bounded by the luminal border. The external elastic cross-sectional areas (EEMCSAs) are the vessel area. Equation (8) is shown as follows:

$$EEMCSA = \frac{\text{Sum(AdventitiaMatrix}(x, y) > 0)}{(\text{ratio}^2)}$$

$$\text{Lumen CSA} = \frac{\text{Sum(IntitiaMatrix}(x, y) > 0)}{(\text{ratio}^2)} \quad (8)$$

where the ratio represents the unit conversion from pixel numbers to mm. In 256×256 images, the ratio is 28.

c) *Atheroma Eccentricity (AE)*: AE reflects the deformation of atherosclerotic plaques. Measurement of atherosclerotic burden and assessment of endothelial function by IVUS is a useful tool for assessing early features of coronary atherosclerosis [25]. The parameters are calculated, as shown in the following equation:

$$AE = \frac{\max AT - \min AT}{\max AT}. \quad (9)$$

AE represents atherosclerotic eccentricity, and AT represents atherosclerotic plaque thickness. The plaque matrix was calculated by the double line segment coverage algorithm, so it is easy to find the maximum plaque thickness and the minimum plaque thickness.

d) *RI*: In restenosis after balloon angioplasty, adventitia thickening and shrinking leads to vascular remodeling and lumen stenosis [26]. The measurement of the RI is critical. The parameter is calculated, as shown in the following equation:

$$RI = \frac{\text{CurrentVesselArea}}{\text{ReferenceVesselArea}} \quad (10)$$

where RI represents the remodeling index. The reference vessel area is the image's vessel area that had the minimum PB.

e) *Lumen Area Stenosis (LAS)*: Obtaining LAS in predicting renal artery vessels has a great reference for predicting hypertension improvement [27]. The parameter is calculated, as shown in the following equation:

$$LAS = \frac{\text{ReferenceLA} - \text{min LA}}{\text{ReferenceLA}} \quad (11)$$

where LAS represents the lumen area stenosis, and LA represents the lumen area. The reference image is the image that has the minimum PB.

IV. EXPERIMENTS AND RESULTS ANALYSIS

A. Data Sets and Experimental Environment

The data used in the experiment came from Qilu Hospital of Shandong University. The hospital provided IVUS images of 25 patients for DeepLabV3+ training. The number of training images was 7188. The age distribution of patients ranged from 56.5 ± 14.5 . The minimum number of images per patient was 100. Therefore, the number of images and the generalization of the images were excellent. The model is also more reliable because it collects raw data from all ages and genders. Additionally, the IVUS data set includes bifurcated vessels and artificial blood vessels. Therefore, the model is more robust than a model with only normal blood vessels. The trained IVUS image is an RGB three-channel image with a size of 256×256 . In the parameter accuracy test experiment, 212 + 173 images of 10 patients were selected and labeled by cardiovascular experts. The images were 256×256 sized RGB three-channel images. Of these, 212 were individually unrelated images from six patients, and 173 were sequence images taken from four patients to test timing parameter accuracy. Continuous image refers to the same section of a blood vessel image at the same sampling frequency. Discontinuous images refer to randomly selecting a certain number of images from all experimental subjects.

The data set is employed to validate the proposed system. The experimental environment is described as follows: Ubuntu 18.04.1 LTS, 16-GB RAM, CPU clocked at 4.0 Hz, and TITAN X graphical processing unit (GPU) with 12-GB memory.

B. Segmentation Results

To test the performance of each automated segmentation network, we have done a comparative test on the data and the results are shown in Table I.

TABLE I
COMPARISON OF FIVE CLASSIC IMAGE SEGMENTATION ALGORITHMS

Index Networks	IoU background	IoU vessel	IoU lumen	Mean IoU
FCN	0.992	0.683	0.900	0.859
GAN	0.979	0.333	0.888	0.733
PSPnet	0.991	0.700	0.873	0.855
Segnet	0.992	0.707	0.873	0.857
U-net	0.992	0.707	0.869	0.856
Deeplab V3+	0.992	0.722	0.908	0.874

TABLE II
DEEPLABV3+ PRETRAIN MODELS COMPARISONS

	Resnet101	Resnet50
IOU vessel	0.722	0.701
IOU lumen	0.908	0.897
IOU Background	0.992	0.992
mIOU	0.874	0.863
Dice vessel	0.826	0.812
Dice lumen	0.946	0.939
Dice Background	0.996	0.996
mDice	0.923	0.916

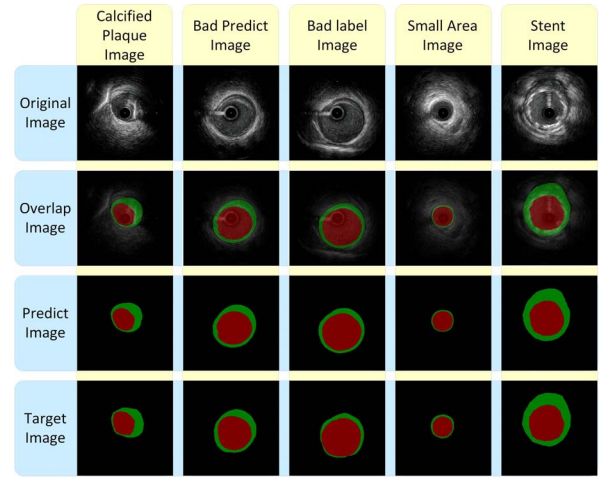


Fig. 10. DeepLabV3+ segmentation output.

The experimental results show that Deeplab V3+ has the highest IoU and achieves the best segmentation effect. In the segmentation experiment of DeepLabV3, the current common ResNet101 [28] and ResNet50 [28] were selected as pre-training models for comparison and verification (Table II). ResNet101 was chosen as the final model of the segmentation algorithm.

The segmentation algorithm had significant prediction errors in small areas (Fig. 10). The small mislabeling of the cardiologist will also produce huge errors. The green area is too small, so doctor's minor mislabeling will be greatly enlarged, resulting in a large EccentricityIndex error.

C. Fully Automatic IVUS Multiparameter Extraction

The experiment calculated 10 parameters of maximum lumen diameter (MaxLD), minimum lumen diameter (MinLD), EEM CSA, lumen cross-sectional areas

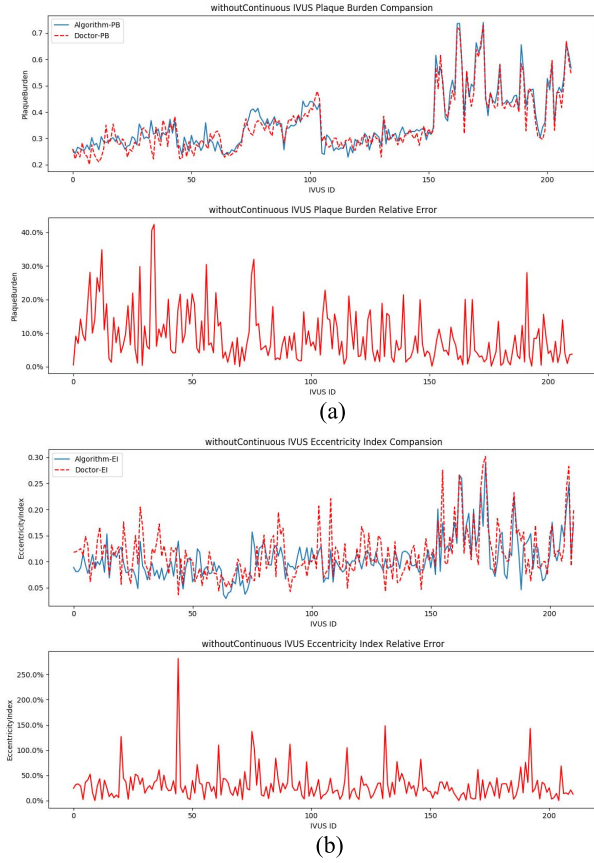


Fig. 11. (a) Comparison of PB without continuity. (b) Comparison of the EI without continuity.

(Lumen CSAs), PB, EI, atherosclerosis eccentricity, minimum lumen area, RI, and lumen area stenosis. The total time processed by the algorithm was 4.7388 imgs/s. The first seven parameters did not require a correlation between images. The last three parameters required correlation between the images. To test the accuracy of the parameter calculations, we first used 212 unrelated IVUS images for partial parameter testing. Equation (8) was used to obtain a relative error with respect to PB. The results are shown in Fig. 11(a) and performed well. The results of the EI are shown in Fig. 11(b). In Fig. 11(b), the overall trend calculated by the algorithm is the same as that of the cardiologist.

IVUS instruments were unable to provide atherosclerosis eccentricity to cardiologists. However, the algorithm herein can provide parameters for atherosclerosis eccentricity. After testing the parameters without image correlation, the remaining three parameters requiring image correlation were tested. RI relative error (Fig. 12) also maintained a small value. The parameters of the minimum lumen area and lumen area stenosis were then tested. These two parameters had only one value in the calculation of a group of images. The result of manual measurement of the minimum lumen area by a cardiologist was 9.320 mm², and the result of a narrow lumen area is shown in Fig. 12. The algorithm measured the minimum lumen area with a result of 9.870 mm², and the lumen area was 0.325 mm², so the relative error of the

TABLE III
COMPARISON OF THE PARAMETER AVERAGE RELATIVE ERROR

	AVE Relative Error with Continuity	AVE Relative Error Without Continuity
PlaqueBurden	10.1%	8.78%
MaxLD	6.78%	4.87%
MinLD	8.49%	6.67%
EEM CSA	7.85%	10.03%
Lumen CSA	9.06	8.41%
EccentricityIndex	30.24%	30.4%
AtheromaEccentricity	-	-
RemodelingIndex	5.91%	-
MinimumLumenArea	6.87%	-
LumenAreaStenosis	9.58%	-

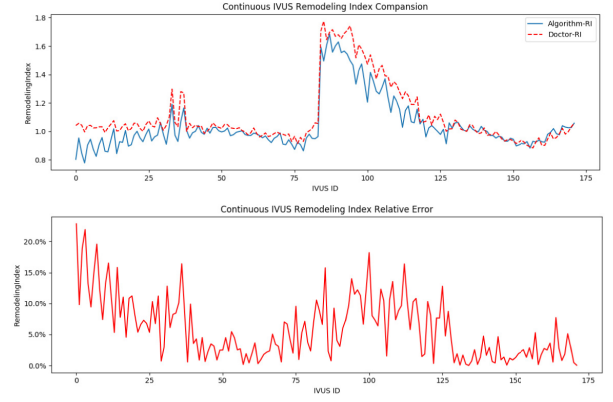


Fig. 12. Comparison of the RI with continuity.

smallest lumen area was 5.90%, and the relative error of the lumen area was 8.45%. The results are shown in Table III. In Table III, in the first column, the first seven parameters can be represented without the correlation between the images. The first five parameters are the main parameters that were primarily tested in our experiments. The last three parameters needed to be obtained by the correlation between the images.

It can be seen from the above of Fig. 11(a) that the resulting graph is consistent with the distribution line graph of the gold standard. In Fig. 11(a) below, there are some high relative errors, which are caused by two reasons: 1) the difference between the segmentation accuracy of the segmentation network and the accuracy of the doctor's manual labeling and 2) as shown in (7), the PB value itself is small. If the EEM CSA and Lumen CSA are relatively close, small vessel area label fluctuations will cause great relative errors.

In Fig. 11(b), as the blood vessels tend to be round, the max LD and min LD which make up the EI parameters are closer than EEM CSA and Lumen CSA. A small value deviation will cause a great relative error. Therefore, doctors pay more attention to the overall data distribution rather than the relative error. As shown in Fig. 11(b): the EI gold standard is consistent with the framework data distribution results.

In Fig. 12, RI requires a reference frame to participate in the numerical calculation when the reference frame selected by the framework is inconsistent with the reference frame selected by the cardiologist; an overall offset phenomenon will occur. For example, IVUS ID80-125 has an upward shift in RI.

TABLE IV
STATISTICAL DIFFERENCE ANALYSIS WITHOUT CONTINUITY

	Mean difference	Standard Error	Confidence Interval	P Value
PB	0.0104	0.0101	(-0.01,0.03)	0.321
MaxLD	0.0243	0.0684	(-0.11,0.16)	0.722
MinLD	0.0727	0.0645	(-0.05,0.19)	0.260
EEM CSA	1.3446	0.5767	(0.21,2.47)	0.052
Lumen CSA	0.4765	0.3507	(-0.21,1.17)	0.175
EI	-0.0084	0.0044	(-0.17,0.001)	0.055

TABLE V
STATISTICAL DIFFERENCE ANALYSIS WITH CONTINUITY

	Mean difference	Standard Error	Confidence Interval	P Value
PB	0.0003	0.0100	(-0.02,0.19)	0.971
MaxLD	-0.0204	0.0902	(-0.19,0.16)	0.821
MinLD	0.0343	0.0819	(-0.12,0.19)	0.675
EEM CSA	0.8993	0.6600	(-0.39,2.19)	0.174
Lumen CSA	0.2554	0.4127	(-0.55,1.07)	0.536
EI	-0.0147	0.0046	(-0.02,0.005)	0.002
RI	-0.0597	0.0219	(-0.102,-0.02)	0.007

To test the accuracy of parameter calculation, this article designs two experiments. One is an experiment of relative error rate, in which the correlation error rate of continuous images and noncontinuous images is shown in Table III. In addition, this article also performed statistical analysis on the parameters obtained by the gold standard and the algorithm, and the results obtained are shown in Tables IV and V.

Through the average relative error table, it can be seen that the algorithm has an excellent guarantee in accuracy except for the EI, because the value of the EI is affected by the MaxLD minus the MinLD. In (6), a small change in the denominator max LD will cause a great change in EI. The distance between max LD and min LD is small, which also causes the relative error of EI to fluctuate greatly. What is more, cardiologists cannot directly calculate the EI from IVUS images. Usually, the IVUS instrument can only automatically acquire the first six parameters. However, with our algorithm, 10 parameters can be obtained. The distribution consistency of the IVUS parameters was compared using the Bland–Altman algorithm, as shown in Fig. 13. All six parameters (MinLD is similar to MaxLD) that appear basically in the figure were the same as those measured by a cardiologist. In summary, the parameters automatically extracted by the framework provide an auxiliary diagnosis for cardiologists.

In Table IV, the p-values of all parameters are greater than 0.05, so there is no statistically significant difference between the data obtained by the gold standard and the algorithm. However, in Table V, all parameters are greater than 0.05 except for EI and RI. The significant difference of EI is the same as the related error, which is the significant difference caused by the relatively small data itself, so we do not output EI as the main parameter. And RI is calculated based on the selected reference frame, and the result will be very different if the reference frame is different. In our algorithm, the reference frame is artificial and not universal. Therefore, RI cannot be

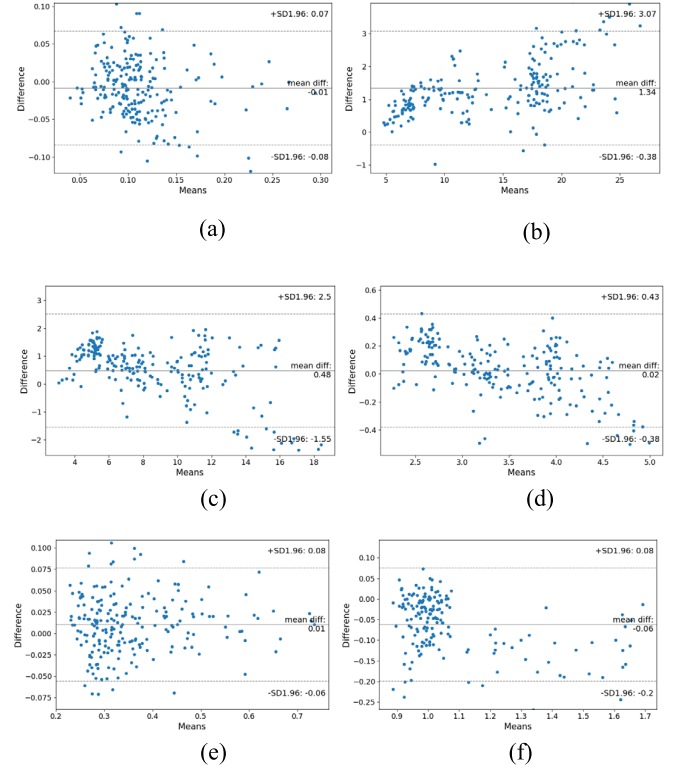


Fig. 13. IVUS parameters Bland–Altman plot. (a) EI. (b) EEM CSA. (c) Lumen CSA. (d) MaxLD. (e) PB. (f) RI.

the output as the main parameter, but only as a reference for clinicians.

V. DISCUSSION AND CONCLUSION

This article provides a fully automated IVUS multiparameter extraction framework and achieves fully automation IVUS parameters extraction. The framework provides up to ten IVUS parameters toward clinical seven IVUS parameters. Moreover, this article provides a multiclass parameter extraction solution for IVUS denoising as data preprocessing. A new algorithm is proposed to obtain basic IVUS parameters from the original IVUS image.

The data set for segmentation training consists of 7188 IVUS images. DeepLabV3+ presegmentation result is 0.874 mIoU, 0.923 mDice, and meet the need for clinical accuracy. The algorithm was tested using IVUS images of 256×256 pixels. All 212 + 173 images were labeled by cardiovascular specialists. About 212 discrete IVUS images were used to test parameters that did not require image correlation. The relative error of the main parameters was not more than 10.1%. The average relative error was 8.08%. The 173 images were related and selected from the same blood vessel of the same patient. The relative error of the main parameters of the continuous image did not exceed 10.03%. The average relative error was 7.734%. After the experiment, the framework's processing speed is 4.7388 imgs/s and obtains 4.007 imgs/s in DeepLabV3+ segmentation which implements real-time parameter acquisition. It can be concluded that the integrated

algorithm can effectively reduce the workload of cardiologists and achieve automatic acquisition of IVUS multiparameters.

However, there are still many aspects for improvement in this article. For example, the accuracy of segmentation is not high enough, resulting in inaccurate parameter calculations. The next step is to improve the segmentation network for precise segmentation of intima and adventitia. In addition, due to the difficulty of medical data collection, the amount of data in this article is still not large enough. The next work should continue to expand the number of data sets, improve the robustness of the algorithm, and build a more complete database.

REFERENCES

- [1] L. Chen, Y. Zhu, G. Papandreou, F. Schroff, and H. Adam, "Encoder-decoder with atrous separable convolution for semantic image segmentation," in *Proc. Eur. Conf. Comput. Vis.*, 2018, pp. 833–851.
- [2] U. Rajendra Acharya *et al.*, "Plaque tissue characterization and classification in ultrasound carotid scans: A paradigm for vascular feature amalgamation," *IEEE Trans. Instrum. Meas.*, vol. 62, no. 2, pp. 392–400, Feb. 2013.
- [3] U. R. Acharya *et al.*, "An accurate and generalized approach to plaque characterization in 346 carotid ultrasound scans," *IEEE Trans. Instrum. Meas.*, vol. 61, no. 4, pp. 1045–1053, Apr. 2012.
- [4] J. Stoitsis, S. Golemati, and K. S. Nikita, "A modular software system to assist interpretation of medical images—Application to vascular ultrasound images," *IEEE Trans. Instrum. Meas.*, vol. 55, no. 6, pp. 1944–1952, Dec. 2006.
- [5] J. Yang, L. Tong, M. Faraji, and A. Basu, "IVUS-net: An intravascular ultrasound segmentation network," 2018, *arXiv:1806.03583*. [Online]. Available: <http://arxiv.org/abs/1806.03583>
- [6] F. S. Zakeri, S. K. Setarehdan, and S. Norouzi, "Automatic media-adventitia IVUS image segmentation based on sparse representation framework and dynamic directional active contour model," *Comput. Biol. Med.*, vol. 89, pp. 561–572, Oct. 2017.
- [7] D. Molony, H. Hosseini, and H. Samady, "TCT-2 deep IVUS: A machine learning framework for fully automatic IVUS segmentation," *J. Amer. College Cardiol.*, vol. 72, no. 13, p. B1, Sep. 2018.
- [8] S. Sun, M. Sonka, and R. R. Beichel, "Graph-based IVUS segmentation with efficient computer-aided refinement," *IEEE Trans. Med. Imag.*, vol. 32, no. 8, pp. 1536–1549, Aug. 2013.
- [9] E. G. P. Bovenkamp, J. Dijkstra, J. G. Bosch, and J. H. C. Reiber, "Multi-agent segmentation of IVUS images," *Pattern Recognit.*, vol. 37, no. 4, pp. 647–663, Apr. 2004.
- [10] L. L. Vercio, M. Del Fresno, and I. Larrabide, "Detection of morphological structures for vessel wall segmentation in IVUS using random forests," *Proc. SPIE*, vol. 10160, Jan. 2017, Art. no. 1016012.
- [11] Z. Rezaei, A. Selamat, A. Taki, M. S. Mohd Rahim, and M. R. Abdul Kadir, "Automatic plaque segmentation based on hybrid fuzzy clustering and k nearest neighborhood using virtual histology intravascular ultrasound images," *Appl. Soft Comput.*, vol. 53, pp. 380–395, Apr. 2017.
- [12] A. Taki *et al.*, "Automatic segmentation of calcified plaques and vessel borders in IVUS images," *Int. J. Comput. Assist. Radiol. Surg.*, vol. 3, nos. 3–4, pp. 347–354, Sep. 2008.
- [13] Y. Chang, L. Yan, M. Chen, H. Fang, and S. Zhong, "Two-stage convolutional neural network for medical noise removal via image decomposition," *IEEE Trans. Instrum. Meas.*, vol. 69, no. 6, pp. 2707–2721, Jun. 2020.
- [14] A. Mencatini, "Mammographic images enhancement and denoising for microcalcification detection using dyadic wavelet processing," in *Proc. IEEE Instrum. Meas. Technol. Conf.*, Dec. 2006, pp. 49–53.
- [15] F. Russo, "Noise removal from image data using recursive neurofuzzy filters," *IEEE Trans. Instrum. Meas.*, vol. 49, no. 2, pp. 307–314, Apr. 2000.
- [16] J. Long, E. Shelhamer, and T. Darrell, "Fully convolutional networks for semantic segmentation," in *Proc. IEEE Conf. Comput. Vis. Pattern Recognit. (CVPR)*, Jun. 2015, pp. 3431–3440.
- [17] H. Zhao, J. Shi, X. Qi, X. Wang, and J. Jia, "Pyramid scene parsing network," in *Proc. IEEE Conf. Comput. Vis. Pattern Recognit. (CVPR)*, Jul. 2017, pp. 2881–2890.
- [18] V. Badrinarayanan, A. Kendall, and R. Cipolla, "SegNet: A deep convolutional encoder-decoder architecture for image segmentation," *IEEE Trans. Pattern Anal. Mach. Intell.*, vol. 39, no. 12, pp. 2481–2495, Dec. 2017.
- [19] O. Ronneberger, P. Fischer, and T. Brox, "U-Net: Convolutional networks for biomedical image segmentation," in *Proc. Int. Conf. Med. Image Comput. Comput.-Assist. Intervent.* Berlin, Germany: Springer, 2015, pp. 234–241.
- [20] S. Zheng *et al.*, "Conditional random fields as recurrent neural networks," in *Proc. IEEE Int. Conf. Comput. Vis. (ICCV)*, Dec. 2015, pp. 1529–1537.
- [21] W. Zaremba, I. Sutskever, and O. Vinyals, "Recurrent neural network regularization," 2014, *arXiv:1409.2329*. [Online]. Available: <http://arxiv.org/abs/1409.2329>
- [22] S. Brugaletta *et al.*, "Comparison of *in vivo* eccentricity and symmetry indices between metallic stents and bioresorbable vascular scaffolds: Insights from the ABSORB and SPIRIT trials," *Catheterization Cardiovascular Interventions*, vol. 79, no. 2, pp. 219–228, Feb. 2012.
- [23] M. Selwaness *et al.*, "Determinants of carotid atherosclerotic plaque burden in a stroke-free population," *Atherosclerosis*, vol. 255, pp. 186–192, Dec. 2016.
- [24] H. Koiwaya *et al.*, "*in vivo* molecular imaging of ruptured coronary atherosclerotic plaque using IVUS, OCT, and FDG-PET/CT," *JACC: Cardiovascular Interventions*, vol. 9, no. 12, pp. e113–e115, Jun. 2016.
- [25] S. H. Han *et al.*, "Sex differences in atheroma burden and endothelial function in patients with early coronary atherosclerosis," *Eur. Heart J.*, vol. 29, no. 11, pp. 1359–1369, Jan. 2008.
- [26] E. Falk, T. Thim, and I. B. Kristensen, "Atherosclerotic plaque, adventitia, perivascular fat, and carotid imaging," *JACC, Cardiovascular Imag.*, vol. 2, no. 2, pp. 183–186, 2009.
- [27] M. A. Leeser *et al.*, "Prediction of hypertension improvement after stenting of renal artery stenosis: Comparative accuracy of transluminal pressure gradients, intravascular ultrasound, and angiography," *J. Amer. College Cardiol.*, vol. 53, no. 25, pp. 2363–2371, 2009.
- [28] K. He, X. Zhang, S. Ren, and J. Sun, "Deep residual learning for image recognition," in *Proc. IEEE Conf. Comput. Vis. Pattern Recognit. (CVPR)*, Jun. 2016, pp. 770–778.



Yankun Cao was born in Heze, Shandong, China, in 1993. She is currently pursuing the Ph.D. degree with the School of Software, Shandong University, Jinan, China.

Her research interest now is pattern recognition and deep learning.



Ziqiao Wang is currently pursuing the master of engineering degree with the School of Information Science and Engineering, Shandong University, Jinan, China.

His research interests include machine learning, deep learning, pattern recognition, and medical image analysis.



Zhi Liu (Member, IEEE) received the Ph.D. degree from the Institute of Image Processing and Pattern Recognition, Shanghai Jiao Tong University, Shanghai, China, in 2008.

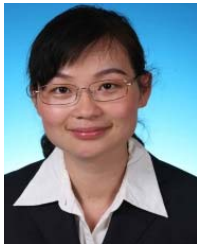
He is an Associate Professor with the School of Information Science and Engineering, Shandong University, Jinan, China. He is the Head of the Intelligent Information Processing Group. His current research interests are in applications of computational intelligence to linked multicomponent Big Data systems, medical images in the neurosciences,

multimodal human–computer interaction, remote sensing image processing, content-based image retrieval, semantic modeling, data processing, classification, and data mining.



Yujun Li (Member, IEEE) received the Ph.D. degree from the Harbin Institute of Technology, Harbin, China, in 2001.

He is currently a Full Professor with the Department of Information Science and Engineering, Shandong University, Jinan, China. His research interests include deep learning, natural language processing, and sentiment analysis.



Xiaoyan Xiao received the Ph.D. degree from Shandong University, Jinan, China, in 2010.

She is a Visiting Scholar with the Harvard Medical School, and an Attending Physician in the Qilu Hospital of Shandong University, Jinan.



Longkun Sun is currently pursuing the medical master's degree in cardiology with the School of Clinical Medicine, Shandong University, Jinan, China.

He is studying in the Qilu Hospital of Shandong University, Jinan, China. His research interest now is echocardiography.



Yang Zhang received the medical degree from Shandong University, Jinan, China, in 2010.

She was a Visiting Scholar of Cornell University, Ithaca, NY, USA, in 2014 and 2015, respectively. She is currently an Associate Chief Physician with the Department of Radiology, Qilu Hospital of Shandong University. She specializes neuroimaging and cardiovascular imaging. She runs two active programs of Neuro-MR research in Shandong University.



Haixia Hou received the Master of Electronics and Communication Engineering degree from Shandong University, Jinan, China, in 2004. She is currently pursuing the Ph.D. degree in information security with the Beijing University of Post and Telecommunications, Beijing, China.

Her main research interests include information security, user cross-domain behavior analysis, and network security.



Pengfei Zhang is a Doctor of Medicine and a Professor. Now, he is the Chief Physician of the Qilu Hospital of Shandong University, Jinan, China. In conformal cardiac ultrasound architecture and its supporting artificial intelligence chips, beam synthesis, ultrasonic image intelligent analysis, ultrasonic conformal material preparation technology, as well as ultrasound engineering and clinical applications, he has published more than 50 SCI papers. It has applied for 18 invention patents and six utility model patents, and has granted six patents and three PCT patents.

Dr. Zhang won the 11th The World Federation of Ultrasound Medicine Award, the 20th Annual Meeting of the American Society of Echocardiography, characteristic original research.



Guang Yang (Member, IEEE) received the B.Eng. degree, the M.Sc. degree in vision imaging and virtual environments from the Department of Computer Science, University College London, London, U.K., in 2006, and the Ph.D. degree in medical image analysis from CMIC, Department of Computer Science and Medical Physics, University College London in 2012.

He is currently an Honorary Lecturer with the Neuroscience Research Centre, Cardiovascular and Cell Sciences Institute, St. George's, University of London. He is also an Image Processing Physicist and an Honorary Senior Research Fellow with the Cardiovascular Research Centre, Royal Brompton Hospital, and also affiliated with the National Heart and Lung Institute, Imperial College London, London.

Dr. Yang is a member of ISMRM and SPIE. (Based on document published on August 17, 2020.)